Acta Metallurgica Sinica (English Letters) (2020) 33:67–74
https://doi.org/10.1007/s40195-019-00932-0

High-Speed Friction Stir Welding of T6-Treated B_4Cp/6061Al Composite

Y. Z. Li[1] · Y. N. Zan[2,3] · Q. Z. Wang[1] · B. L. Xiao[2] · Z. Y. Ma[2]

Received: 13 May 2019 / Revised: 5 June 2019 / Published online: 17 July 2019
© The Chinese Society for Metals (CSM) and Springer-Verlag GmbH Germany, part of Springer Nature 2019

Abstract
T6-treated 20 wt% B_4Cp/6061Al sheets were joined under welding speeds of 400–1200 mm/min by friction stir welding (FSW) with a threaded cermet pin. The macro-defect-free FSW joints could be achieved at high welding speeds up to 1200 mm/min, but larger plunge depth was required at the welding speeds of 800 and 1200 mm/min to eliminate the tunnel defect. In the nugget zone (NZ) of the joints, the B_4C particles were broken up and uniformly redistributed. The NZ exhibited lower hardness than the base metal (BM), and the hardness value almost did not change with increasing welding speed, attributable to the dissolution of precipitates. Compared with the BM, the joints showed lower tensile strength. As the welding speed increased from 400 to 800 mm/min, the joint efficiencies were nearly the same and up to ~ 73%. When the welding speed increased up to 1200 mm/min, the tensile strength significantly decreased, due to the occurrence of kissing bond defect at the bottom of the NZ. With increasing welding speed, the fracture location of the joints transferred gradually from the heat-affected zone to the NZ due to the kissing bond defects.

Keywords Metal-matrix composites · Microstructures · Mechanical properties · Friction stir welding · High-speed welding

1 Introduction

B_4C particle (B_4Cp)-reinforced aluminum matrix composites (B_4Cp/Al) have recently been considered as an alternative to the common particles (SiCp, Al_2O_3p, etc.)-reinforced composites for some structural applications due to the lower density to hardness ratio of B_4Cp [1, 2]. Particularly, the neutron capture ability of B_4Cp makes the B_4Cp/Al an ideal neutron absorbing material for nuclear applications [3, 4], in which the welded structures are indispensable.

Friction stir welding (FSW) is a highly feasible welding technique for the composites to avoid the fusion welding defects [5, 6], and homogenize the distribution of the reinforcement as well [4, 7]. This technique is also widely used for the fabrication and modification of metal-matrix composites [4, 8]. However, the ultra-hard reinforcements result in the poor plastic deformation ability of the composites [9, 10], which makes it difficult to realize the high-speed welding. Furthermore, studies on FSW of B_4Cp/Al were limited and mostly focused on the softer B_4Cp/Al [11, 12]. For the high-performance applications, the precipitation-strengthened composites such as the B_4Cp/6061Al-T6 with higher strength are required. In this case, the FSW of such high-strength composites needs to be deeply explored.

In general, the precipitates, being a critical factor to determine the properties of the precipitation-strengthened aluminum alloys, would suffer dissolution, reprecipitation and/or coarsening during FSW [13], leading to the softening of the joints. It was documented that the FSW softening could be moderated by increasing welding speed [14]. This offers the possibility to obtain high-quality joints with high joint efficiency by high-speed FSW. In particular, the nearly

Available online at http://link.springer.com/journal/40195

✉ Q. Z. Wang
qzhwang@imr.ac.cn

✉ Z. Y. Ma
zyma@imr.ac.cn

[1] Key Laboratory of Nuclear Materials and Safety Assessment, Institute of Metal Research, Chinese Academy of Sciences, 72 Wenhua Road, Shenyang 110016, China

[2] Shenyang National Laboratory for Materials Science, Institute of Metal Research, Chinese Academy of Sciences, 72 Wenhua Road, Shenyang 110016, China

[3] University of Science and Technology of China, Shenyang 110016, China

equal strength joint to the base material of SiCp/2009Al was achieved at a high welding speed of 800 mm/min by Wang et al. [15]. However, whether increasing the speed of FSW could produce increased joint efficiency in the composites based on 6xxx series aluminum alloys such as 6061 is still unclear [16, 17].

The precipitation behavior of the precipitation-strengthened composites was similar to the corresponding matrix alloys, however, with accelerated kinetics and much finer precipitates [18, 19], which may lead to different evolutions during FSW. In addition, the precipitation characteristics were quite different for different aluminum alloys. For example, the 2xxx series aluminum alloys exhibit a strong tendency for natural aging, whereas the 6xxx series aluminum alloys do not have this inclination. The precipitation characteristic differences could lead to varied precipitate evolution during FSW, especially the responses to welding speed [20, 21]. Because the composites based on the 6xxx series aluminum alloys exhibit lower strength and higher ductility compared to those based on the 2xxx series ones, it is expected that higher welding speeds could be applied for the composites based on the 6xxx series aluminum alloys.

In our previous study [22], the sound joints of 20 wt% B_4Cp/6061Al-T6 were achieved at welding speeds of 50–400 mm/min, and improved joint strength was obtained with increasing welding speed. In this work, the 20 wt% B_4Cp/6061Al-T6 was subjected to FSW at higher welding speeds up to 1200 mm/min, aimed to (a) study the feasibility of achieving sound FSW joints at higher speeds and (b) clarify the effect of the welding speed on the microstructure and mechanical properties.

2 Experimental

20 wt% B_4Cp/6061Al-T6 sheets 2.9 mm in thickness were used in this work. The B_4Cp/Al billet was fabricated by powder metallurgy technique, including the powder mixing and hot pressing, using 6061Al alloy as the matrix and B_4Cp as the reinforcement. The billet was hot-extruded and followed by hot rolling to a thickness of 2.9 mm. The sheets were solutionized at 530 °C for 2.5 h, water-quenched and then aged at 175 °C for 8 h to achieve T6 temper condition. Detailed fabrication process of the composite has been described in our previous study [22].

The T6-sheets were butt-welded along the rolling direction using an FSW machine at a rotation rate of 1000 rpm and welding speeds of 400, 800 and 1200 mm/min, denoted as joints 400, 800-I and 1200-I in the following text. A plunge depth of 0.15 mm and a tool axial tilting angle of 2° were used for all FSW processes. An ultra-hard cermet tool with a shoulder 14 mm in diameter and a threaded conical-shaped pin 5 mm in root diameter and 2.8 mm in length was used for FSW.

During welding experiments, it was found that it was difficult to obtain sound joints at welding speeds of 800 and 1200 mm/min with the plunge depth of 0.15 mm. To ensure the high quality of the joints, the additional plunge depths of 0.2 mm and 0.4 mm were applied for 800 and 1200 mm/min, respectively. The corresponding joints are denoted as joints 800-II and 1200-II in the following text.

After welding, the FSW joints were cross sectioned perpendicular to the welding direction for microstructural examination by optical microscopy (OM) and scanning electron microscopy (SEM) after it was mechanically polished and etched by Keller's reagent. The differential scanning calorimetry (DSC) was conducted to characterize the precipitation features in the base material (BM) and the different FSW joints, by measuring the heat evolution during the heating, with a heating rate of 10 °C/min. Five specimens of 50 mg in weight were tested, i.e., the solutionized BM (BM-Sol), the T6-treated BM (BM-T6) and the NZs of joints 400, 800-II and 1200-II (400-NZ, 800-NZ and 1200-NZ, respectively).

The hardness profiles of the joints were measured along the mid-thickness of the cross sections perpendicular to the welding direction under a 1000 gf load for 30 s. The line for the test started from the weld center and extended to 20 mm on both the retreating side (RS) and advancing side (AS). The indentation interval was chosen to be 1 mm. Dog-bone-shaped tensile specimens with a gauge length of 40 mm and a width of 10 mm were machined perpendicular to the welding direction with the NZ being in the center of the gauge. Room-temperature tensile tests were carried out at a strain rate of 1×10^{-3} s^{-1}, and the property data for each condition were obtained by averaging three testing results. The fracture surfaces of the tensile specimens were observed by SEM.

3 Results and Discussion

Figure 1 presents the welding tool morphologies before and after all the FSW operations, with the total welding distance reaching 1000 mm. Slight abrasion on the top and the screw thread of the pin, with almost no shortening of the pin, was observed, indicating the high durability of this self-designed cermet tool for the FSW of the high-strength 20 wt% B_4Cp/6061Al-T6 at high welding speeds up to 1200 mm/min.

Figure 2 shows the surface morphologies of the FSW joints at various welding speeds (v) and various plunge depths for $v = 800$ mm/min and $v = 1200$ mm/min. The smooth surfaces with semicircular features resulting from wake effect were obtained for all the joints. No defects were observed for the joints at 400 and 800 mm/min. For joint

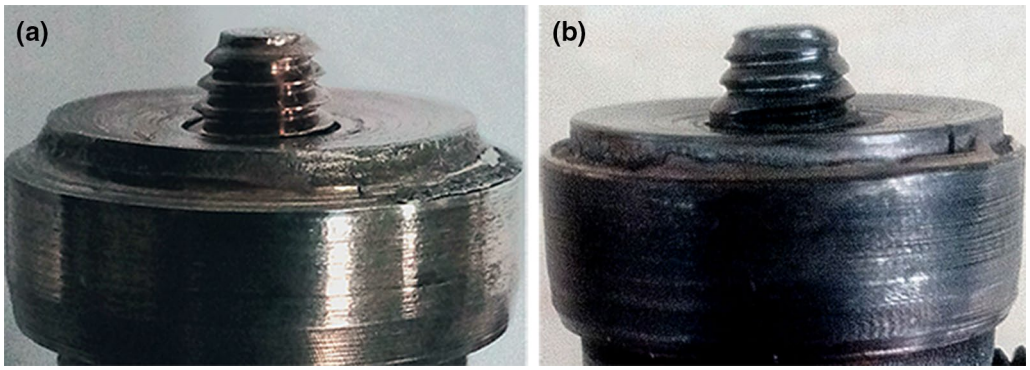

Fig. 1 Welding tools **a** before, **b** after all welding operations

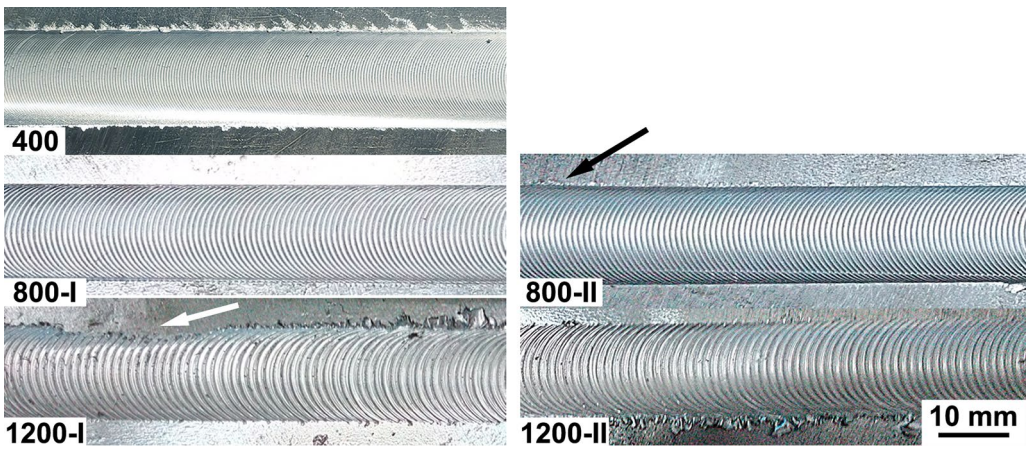

Fig. 2 Surface of the FSW joints at various welding speeds and various plunge depths

1200-I, the incomplete semicircular features were observed due to the insufficient plunge depth, as shown by the white arrow. As the additional plunge depths were applied, larger trimming was generated in joint 800-II, as shown by the black arrow, and the incomplete semicircular features were eliminated in joint 1200-II.

Figure 3a presents the cross-sectional morphologies of the FSW joints under various welding speeds (v) and various plunge depths for $v = 800$ mm/min and $v = 1200$ mm/min. As shown in Fig. 3a, the actual plunge depths were smaller than the preset plunge depths for the joints at $v = 800$ mm/min and $v = 1200$ mm/min, no matter with or without the additional plunge depths. This could be attributed to larger material springback due to the larger elastic deformation amount of the material in the joint region at lower heat input with higher welding speeds.

Figure 3b and c shows the zoom-in morphologies of the white boxes in Fig. 3a. The joints were divided into four zones: nugget zone (NZ), thermomechanically affected zone (TMAZ), heat-affected zone (HAZ) and base material (BM). The NZ widths were almost the same for three welding speeds, without clear NZ/TMAZ boundaries on the RS. Since the width of the TMAZ was too small, it was hard to clearly show the NZ/TMAZ and TMAZ/HAZ boundaries in Fig. 3a.

Sound joint was achieved for joint 400, while tunnel defects were detected for joints 800-I and 1200-I, when the same plunge depths were applied. As shown by the white arrows in Fig. 3b and c, the tunnel defect was only observed at the NZ/HAZ boundary on the RS at the bottom of the NZ for joint 800-I, while for joint 1200-I the tunnel defects were observed both at the NZ/HAZ boundary and in the center of the NZ at the bottom of the NZ. The size of the tunnels was larger in joint 1200-I than in joint 800-I.

The tunnel defect is a common defect in FSW joints when the improper parameters were applied, due to the low heat input, insufficient material plasticization and imbalance in the material flow around the pin [23]. When the lower welding speed $v = 400$ mm/min was used, a long stirring time and consequently adequate material flow resulted in a balanced material flow in the joint. Therefore, a sound FSW joint was produced at $v = 400$ mm/min as shown in Fig. 3a. As the

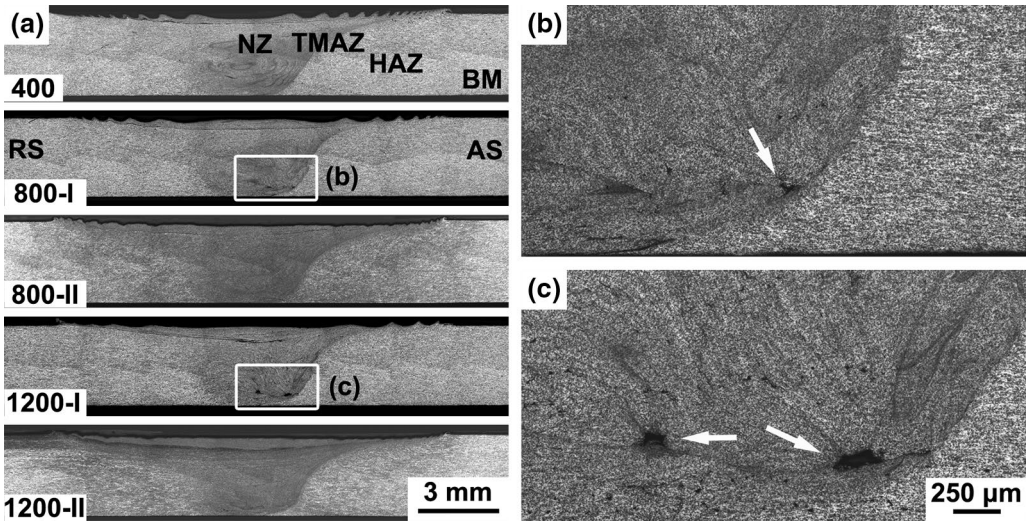

Fig. 3 **a** Cross-sectional macrostructures of FSW joints under various welding speeds and plunge depths, **b**, **c** magnified views of joints 800-I and 1200-I

welding speed increased to 800 and 1200 mm/min, this balanced material flow would be changed into insufficient material flow, due to much higher traveling speed and the poor material plasticization under the decreased heat input. By applying the additional plunge depth at both $v = 800$ mm/min and $v = 1200$ mm/min, the sound joints were achieved by completely eliminating the tunnel defects, as shown in joints 800-II and 1200-II in Fig. 3a, attributing to the increased heat input and the corresponding improved material plasticization under larger plunge depth [24].

Figure 4a–d shows the microstructures of the BM and NZ of the FSW joints with the corresponding B_4Cp size and aspect ratio shown in Fig. 4e. In the BM, the B_4Cp was in a polygonal shape with sharp tips. Some particles with large aspect ratio were observed in the BM. The B_4Cp size was about 7.5 μm with the aspect ratio of about 2.2 (Fig. 4e). The B_4Cp distribution in the BM was slightly non-uniform. The particle clusters [zone (1) in Fig. 4a] and the slightly banded distribution regions of B_4Cp [zone (2) in Fig. 4a] were observed in the BM.

After FSW, the shape of the B_4Cp hardly changed. However, the B_4Cp was redistributed uniformly in the matrix and the number of the B_4Cp with large aspect ratio was decreased in the NZ, resulting from the drastic plastic deformation of the Al alloy matrix and the particle/tool interaction, such as collision, during FSW [4, 25, 26]. Furthermore, the B_4Cp size and aspect ratio were significantly reduced in the NZ as shown by the statistical result (Fig. 4e), with some fine B_4Cp being observed as shown by the white circles in Fig. 4b–d. This indicates that the material flow combined with the interaction between B_4Cp and the welding tool resulted in the fragmentation of B_4Cp during FSW. With increasing welding speed, the distribution, size and aspect ratio of B_4Cp were almost unchanged, indicating a similar impact level of FSW on B_4Cp under such high welding speeds.

Figure 5 shows the DSC curves of the BM with different tempers and the NZs at different welding speeds. Two exothermic peaks located in the range of 200–300 °C were observed for the BM-Sol and all the joints, which were believed to associate with the precipitation of the β'' and β' phases [13]. Only β' precipitates peak was observed for the BM-T6, indicating that most of the precipitates in the BM were β'' phases. It can also be seen in Fig. 5 that the intensities of both the two peaks in the NZs were lower than those in the BM-Sol, and slightly increased with the increasing welding speed from 400 to 800 mm/min and then almost unchanged with the further increase in the welding speed from 800 to 1200 mm/min.

According to our previous study [22], the joint suffered the dissolution of the β'' precipitates, reprecipitation of the spherical-shaped GP-I zone, β'' to β' transformation and coarsening of β'' and β' during FSW. The similar profiles between the FSW joints and the BM-Sol, and the difference between the FSW joints and the BM-T6 indicated that the β'' precipitates in the BM dissolved during FSW and reprecipitated with the same sequence of the BM-Sol during the DSC test. The lower intensity of the β'' precipitate peak, corresponding to lower number of solutes in the NZs compared to the BM-Sol, and the lower intensity of the β' precipitate peak, corresponding to decreased β'' to β' transformation in the NZs during the DSC test, indicated that reprecipitation, β'' to β' transformation and/or coarsening of β'' and β' also occurred accompanied with the dissolution of β'' during FSW.

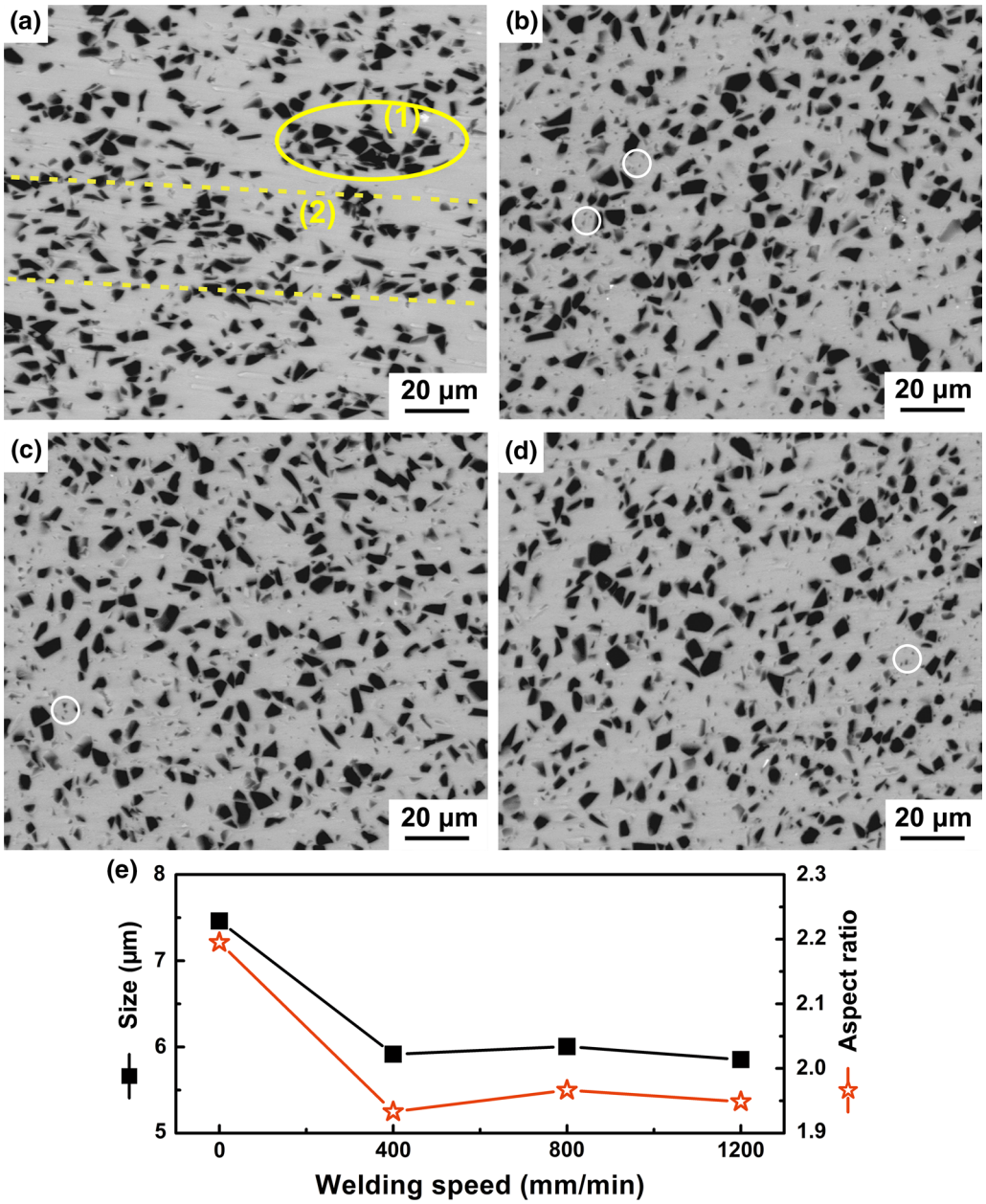

Fig. 4 Microstructures in the BM and in the NZ of FSW joints: **a** BM, **b** joint 400, **c** joint 800-II, **d** joint 1200-II, **e** B_4Cp size and aspect ratio

In general, the heat input and material deformation decreased with increasing welding speed [27], which may decrease the dissolution of the β'' precipitates. However, the slight increase in the peak intensities with increasing welding speed shown in Fig. 5 was observed, indicating that a larger number of solutes was retained in the NZs of joints 800-II and 1200-II after FSW. This might be explained that, as the welding speed increased from 400 to 1200 mm/min, the heat input slightly decreased, which was not enough to trigger the significant difference of the precipitation evolution in the NZs. The additional plunge depth in joints 800-II and 1200-II led to increased heat input which resulted in a similar amount of dissolution of β'' during FSW.

During the cooling down of the joints after FSW, the increased welding speed led to higher cooling rate, resulting in less reprecipitation of β''. Therefore, more solutes were retained in joints 800-II and 1200-II. The slightly increased intensity of the β' precipitates peak in joint 800-II than in joint 400 indicated that more β'' to β' transformation and/or coarsening of β'' and β' occurred during FSW, attributable to the slightly decreased heat input and higher cooling rate in joint 800-II.

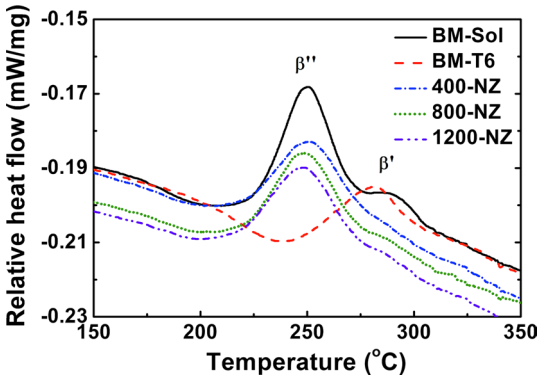

Fig. 5 DSC curves of the BM and the NZs of FSW joints

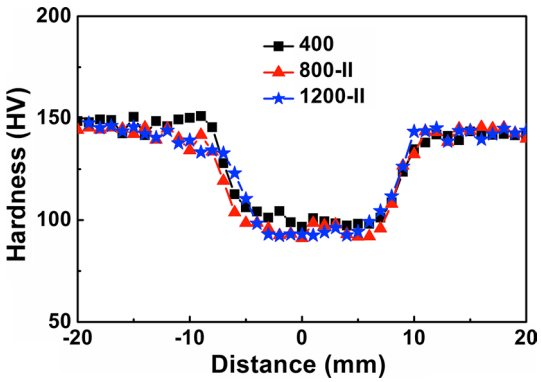

Fig. 6 Transverse cross-sectional hardness profiles of FSW joints

The accelerated precipitation kinetics and the much finer *β″* precipitates in this composite as observed in our previous study [22] may also contribute to decreasing the precipitation evolution difference at various welding speeds, due to the high proneness to dissolve and coarsen under the heat effect.

Figure 6 shows the transverse cross-sectional hardness profiles of joints 400, 800-II and 1200-II. The hardness of the T6-treated BM was about 150 HV. The hardness profiles under different welding speeds showed almost the same patterns and values. A wide low-hardness region was generated in the center of all the joints, in which the hardness was reduced to around 100 HV, and then gradually increased to 150 HV with increasing the distance away from the edges of the low-hardness region. The hardness profiles in the low-hardness region for all the joints were almost flat, with a slightly lower hardness zone (LHZ) at the edges of this region.

The hardness decrease in the joints could be mainly attributed to the dissolution and coarsening of the precipitates [28]. According to the analyses above, the increasing welding speed only resulted in a negligible difference of the precipitation in the NZs when the larger plunge depth was applied at higher welding speeds. Thus, almost the same hardness profiles of all the joints were obtained under three welding speeds.

Figure 7 shows the tensile properties, the engineering stress–strain curves and the corresponding fracture locations of the BM and joints 400, 800-II and 1200-II. The strength of the joints was lower than that of the BM, with almost the same strength and elongation for joints 400 and 800-II, and similar stress–strain curves as well. However, joint 1200-II exhibited much lower strength and elongation. For joint 400, three tensile specimens fractured all in the HAZ; for joint 800-II, two tensile specimens fractured in the HAZ and one in the NZ; for joint 1200-II, all three tensile specimens failed in the NZ, indicating the gradual transformation of the fracture location from the HAZ to the NZ with increasing welding speed as shown in Fig. 7c, in which the white line shows the weld centerline.

Figure 8 shows the representative fractographs. For the joints fracturing at the HAZ, for both joints 400 and 800-II, the ductile fracture surface showed similar features of the BM. For the joints fracturing at the NZ, for both joints 800-II and 1200-II, some holes with sizes of 50–100 μm were observed at the NZ bottom, which were considered as the fracture initiation from the crack propagation features as shown in Fig. 8c and d. The magnified images around the holes indicated that the kissing bond occurred in this region, as shown in Fig. 8e and f.

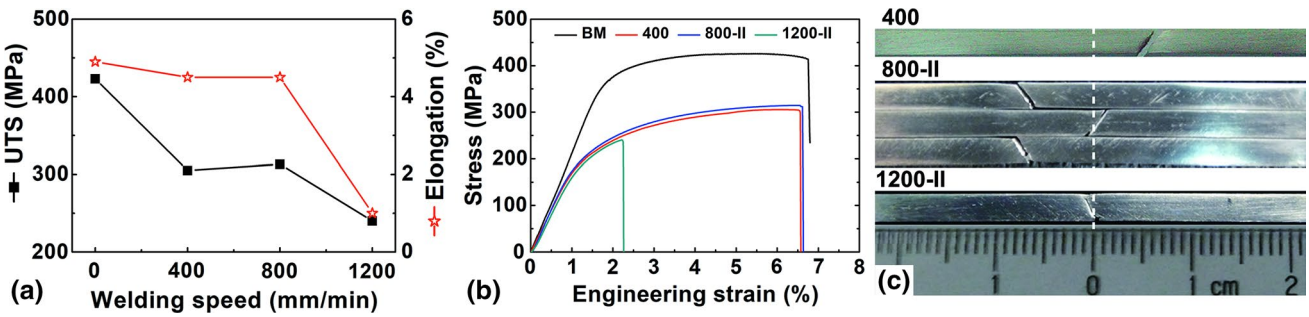

Fig. 7 **a** Tensile properties, **b** engineering stress–strain curves of the BM and FSW joints, **c** the fracture locations of the joints after tensile test

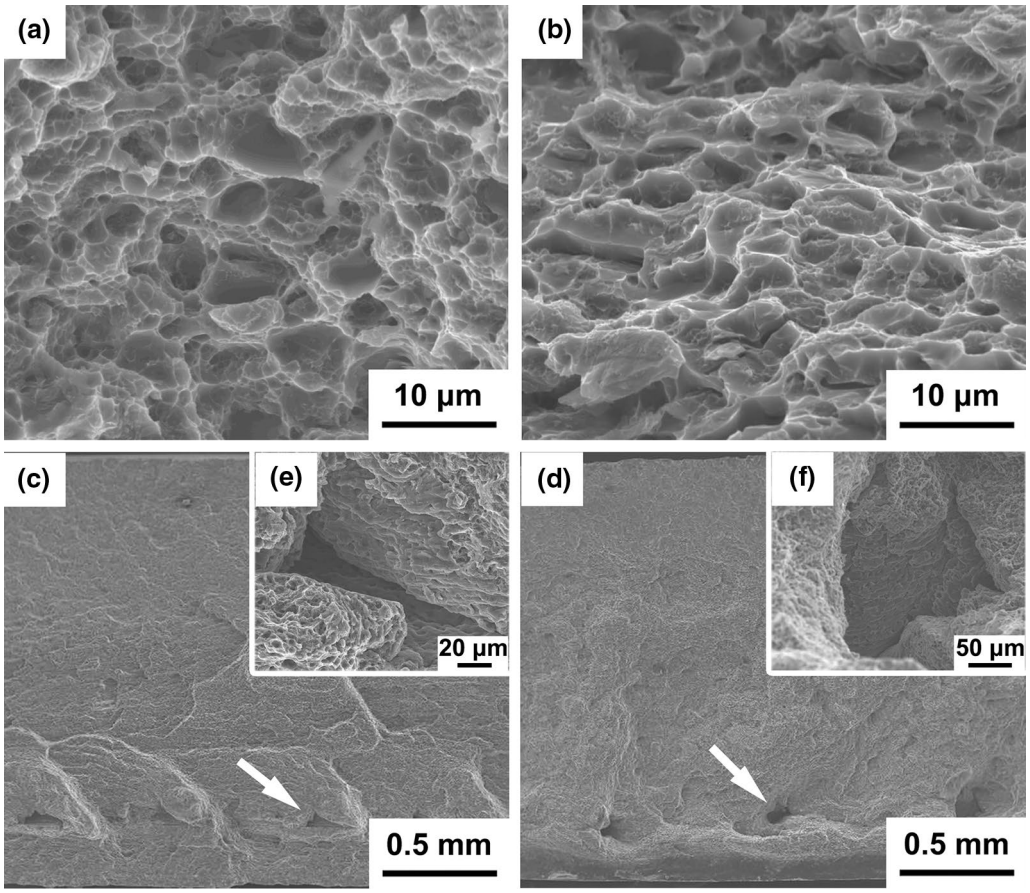

Fig. 8 Fractographs of FSW joints: **a** BM, **b** joint 800-II, HAZ, **c** joint 800-II, NZ, **d** joint 1200-II, NZ. **e**, **f** are the magnified images around the holes pointed out by the white arrows in **c**, **d**, respectively

For joint 400, the decreased strength compared to the BM and the fracture location was consistent with the hardness profile. The close strength of joints 400–800-II was also consistent with the similar hardness profiles of these two joints. With the increase in the welding speed up to 1200 mm/min, the significant decrease in the strength and elongation was attributed to the kissing bond defects, which resulted from the insufficient plastic deformation [29, 30]. Actually, the kissing bond defect was also observed in joint 800-II, as shown in Fig. 8c. This indicates that although the additional plunge depths applied in this study were enough to eliminate the tunnel defects, the kissing bond defects could not be avoided completely at higher welding speeds. Even larger plunge depths might be necessary to eliminate the kissing bond defect at higher welding speeds of 800 and 1200 mm/min.

4 Conclusions

1. Macro-defect-free FSW joints of 20 wt% B_4Cp/6061Al-T6 composites were obtained at high welding speeds up to 1200 mm/min. The additional depths of 0.2 mm and 0.4 mm for 800 and 1200 mm/min, respectively, were necessary to eliminate the tunnel defects.
2. The hardness of the NZ was lower than that of the BM due to the dissolution and coarsening of the precipitates. The joint hardness profiles and hardness values were almost the same at various welding speeds.
3. The tensile strength of the joints was lower than that of the BM and almost the same as the welding speed increased from 400 to 800 mm/min, with the joint efficiency up to ~73% being obtained. The joint strength and elongation at 1200 mm/min were significantly reduced by the kissing bond at the NZ bottom.
4. The fracture location of the joints gradually transferred from the HAZ to the NZ with increasing welding speed due to the kissing bond at higher welding speeds.

Acknowledgements The authors gratefully acknowledge the support of the National Natural Science Foundation of China under Grant Nos. U1508216 and 51771194, and the National Key R & R Program of China under grant No. 2017YFB0703100.

References

[1] S. Gangolu, A.G. Rao, N. Prabhu, V.P. Deshmukh, B.P. Kashyap, Mater. Des. **53**, 581–587 (2014)
[2] A. Kumar, R.N. Rai, IOP Conf. Ser. Mater. Sci. Eng. **377**, 012092 (2018)
[3] Y. Li, W. Wang, J. Zhou, H. Chen, P. Zhang, J. Nucl. Mater. **487**, 238–246 (2017)
[4] M. Paidar, O.O. Ojo, H.R. Ezatpour, A. Heidarzadeh, Surf. Coat. Technol. **361**, 159–169 (2019)
[5] R.S. Mishra, Z.Y. Ma, Mater. Sci. Eng. R **50**, 1–78 (2005)
[6] G.K. Padhy, C.S. Wu, S. Gao, J. Mater. Sci. Technol. **34**, 1–38 (2018)
[7] Y. Huang, J. Li, L. Wan, X. Meng, Y. Xie, Mater. Sci. Eng. A **732**, 205–211 (2018)
[8] G. Huang, W. Hou, Y. Shen, Mater. Charact. **138**, 26–37 (2018)
[9] O.S. Salih, H. Ou, X. Wei, W. Sun, Mater. Sci. Eng. A **742**, 78–88 (2019)
[10] A. Hosseinzadeh, G.G. Yapici, Mater. Sci. Eng. A **731**, 487–494 (2018)
[11] J.F. Guo, P. Gougeon, X.G. Chen, Sci. Technol. Weld. Join. **17**, 85–91 (2012)
[12] X.G. Chen, M. da Silva, P. Gougeon, L. St-Georges, Mater. Sci. Eng. A **518**, 174–184 (2009)
[13] G.R. Cui, D.R. Ni, Z.Y. Ma, S.X. Li, Metall. Mater. Trans. A **45**, 5318–5331 (2014)
[14] S. Prabhu, A.K. Shettigar, K. Rao, S. Rao, M. Herbert, Mater. Sci. Forum **880**, 50–53 (2017)
[15] D. Wang, Q.Z. Wang, B.L. Xiao, Z.Y. Ma, Mater. Sci. Eng. A **589**, 271–274 (2014)
[16] K. Kalaiselvan, N. Murugan, Trans. Nonferrous Met. Soc. China **23**, 616–624 (2013)
[17] M.F. Nikoo, H. Azizi, N. Parvin, H.Y. Naghibi, J. Manuf. Process. **22**, 90–98 (2016)
[18] C. Wu, K. Ma, D. Zhang, J. Wu, S. Xiong, G. Luo, J. Zhang, F. Chen, Q. Shen, L. Zhang, E.J. Lavernia, Sci. Rep. **7**, 9589 (2017)
[19] Y. Zhao, X. Ma, X. Zhao, H. Chen, X. Liu, J. Alloys Compd. **726**, 1053–1061 (2017)
[20] Z. Zhang, B.L. Xiao, Z.Y. Ma, J. Mater. Sci. **47**, 4075–4086 (2012)
[21] F. Fadaeifard, K.A. Matori, S. Abd Aziz, L. Zolkarnain, M.A.Z.B. Abdul Rahim, Metals **7**, 48 (2017)
[22] Y.Z. Li, Y.N. Zan, Q.Z. Wang, B.L. Xiao, Z.Y. Ma, J. Mater. Process. Technol. **273**, 116242 (2019)
[23] N.Z. Khan, A.N. Siddiquee, Z.A. Khan, S.K. Shihab, J. Alloys Compd. **648**, 360–367 (2015)
[24] Z. Zhang, B.L. Xiao, Z.Y. Ma, Mater. Charact. **106**, 255–265 (2015)
[25] V.K. Parikh, A.D. Badgujar, N.D. Ghetiya, Mater. Manuf. Process. **34**, 123–146 (2019)
[26] L.H. Wu, X.B. Hu, X.X. Zhang, Y.Z. Li, Z.Y. Ma, X.L. Ma, B.L. Xiao, Acta Mater. **166**, 371–385 (2019)
[27] A. Barbini, J. Carstensen, J.F. dos Santos, J. Mater. Sci. Technol. **34**, 119–127 (2018)
[28] J. Zhang, X.S. Feng, J.S. Gao, H. Huang, Z.Q. Ma, L.J. Guo, J. Mater. Sci. Technol. **34**, 219–227 (2018)
[29] G. Wang, Y. Zhao, Y. Hao, J. Mater. Sci. Technol. **34**, 73–91 (2018)
[30] X. Liu, H. Liu, T. Wang, X. Wang, S. Yang, J. Mater. Sci. Technol. **34**, 102–111 (2018)